J. Fluid Mech. (2005), *vol.* 537, *pp.* 415–431.
doi:10.1017/S0022112005005495 Printed in the United Kingdom

The Rayleigh–Taylor instability of two-dimensional high-density vortices

By L. JOLY[1], J. FONTANE[1] AND P. CHASSAING[1,2]

[1]ENSICA, 1 Place Émile Blouin, 31056 Toulouse, France

[2]Institut de Mécanique des Fluides, Allée du Prof. C. Soula, 31000 Toulouse, France

(Received 14 September 2004 and in revised form 21 March 2005)

We investigate the stability of variable-density two-dimensional isolated vortices in the frame of incompressible mixing under negligible gravity. The focus on a single vortex flow stands as a first step towards vortex interactions and turbulent mixing. From heuristic arguments developed on a perturbed barotropic vortex, we find that high-density vortices are subject to a Rayleigh–Taylor instability. The basic mechanism relies on baroclinic vorticity generation when the density gradient is misaligned with the centripetal acceleration field. For Gaussian radial distributions of vorticity and density, the intensity of the baroclinic torque due to isopycnic deformation is shown to increase with the ratio δ/δ_ρ of the vorticity radius to the density radius. Concentration of mass near the vortex core is confirmed to promote the instability by the use of an inviscid linear stability analysis. We measure the amplification rate for the favoured azimuthal wavenumbers $m = 2, 3$ on the whole range of positive density contrasts between the core and the surroundings. The separate influence of the density-contrast and the radius ratio is detailed for modes up to $m = 6$. For growing azimuthal wavenumbers, the two-dimensional structure of the eigenmode concentrates on a ring of narrowing radial extent centred on the radius of maximum density gradient. The instability of the isolated high-density vortex is then explored beyond the linear stage based on high-Reynolds-number numerical simulations for modes $m = 2, 3$ and a moderate density contrast $C_\rho = 0.5$. Secondary roll-ups are seen to emerge from the nonlinear evolution of the vorticity and density fields. The transition towards m smaller vortices involves vorticity exchange between initially-rotating dense fluid particles and the irrotational less-dense medium. It is shown that baroclinic enstrophy production is associated with the centrifugal mass ejection away from the vortex centre.

1. Introduction

Baroclinic vorticity production has been identified as the counterpart of buoyancy forces in stratified geophysical flows where misalignment between the gravity acceleration field and the density gradient produces and destroys vorticity, see Turner (1973). The baroclinic vorticity production has been much less commented on in high-Froude-number mixing flows. The transition stage of such flows has deserved some interest since the experimental evidence shows that low-density jets develop specific instability modes (Monkewitz & Sohn 1988). The development of the Kelvin–Helmholtz instability in high-Froude-number incompressible variable-density mixing layers was later subjected to numerical simulations by Soteriou &

Ghoniem (1995), revealing the crucial role of baroclinic vorticity sources. Reinaud, Joly & Chassaing (2000) found a secondary instability in the variable-density mixing layer providing a two-dimensional spatial cascade towards smaller scales. It was demonstrated to be related to the instability of the strained layer of vorticity and density-gradient.

Turner (1957) mentioned the stabilizing effect of the centrifugal force due to rotation within vortex rings lighter than the surrounding medium. He compared it to the action of gravity on stably stratified shear flows. Chomiak & Nisbet (1995) referred briefly to the instability of denser vortices into their variable-density turbulence model. The two-dimensional direct numerical simulations by Chassaing *et al.* (1997) also confirmed the robustness of low-density vortices and the short life-time of high-density vortices. Additional simulations of binary-mixing two-dimensional turbulence, summarized in Joly (2002), described the underlying process of mass-segregation by vorticity measuring negative correlation $\overline{\xi^2\rho'}$, with ξ the vorticity and ρ' the density fluctuation. Also displayed in Joly (2002) were accompanying nonlinear simulations of isolated vortices showing axisymmetrization of a low-density vortex and the blow-up of a high-density vortex into fine-grained smaller structures. Miller, Lindstrom & Cook (2003) observed such a two-dimensional mechanism in the case of an impulsively started density interface at high Schmidt number. After a first roll-up into a primary structure embedding folded density spirals, this mechanism was responsible for a secondary vorticity baroclinic generation. This secondary instability, resulting from the streamline curvature, is of the same type as that occurring in the case of an isolated high-density vortex.

The stability of swirling flows has also attracted much attention owing to the interest in the breakdown of trailing vortices. Both axisymmetric and non-axisymmetric perturbations of swirling flows were analysed in the light of both asymptotic and normal-mode analysis. Though a sufficient condition for centrifugal instability has been extended to the compressible case by Eckhoff (1984) in the limit of large axial wavenumbers, it is demonstrated in a complementary paper by Sipp *et al.* (2005) that such a condition cannot be formulated for two-dimensional non-axisymmetric perturbations. Only an asymptotic analysis in the limit of vanishing density contrast and radius ratio, yields that vortices are unstable to non-axisymmetric perturbations if the density decreases radially somewhere. In contrast with these studies relying on the formulation of classical Sturm–Liouville eigenvalue problems, the present paper favours a heuristic approach and explores the mechanism of the two-dimensional instability of heavy vortices in the light of baroclinic vorticity generation associated with the centripetal acceleration field. This mechanism, originally discussed in Joly (2002), is demonstrated to be of the same nature as the Rayleigh–Taylor instability in an unstable atmosphere. It is explained in the preliminary part of § 2 for a perturbed density field providing a tractable expression of the baroclinic torque associated with departure from barotropy. It succeeds in stressing the destabilizing role of density concentration near the vortex centre. The second part of § 2 is then devoted to the derivation of a inviscid linear stability analysis of the heavy Lamb–Oseen vortex. The growth rate and spatial structure of the eigenmodes, corresponding to the more amplified first azimuthal wavenumbers, are detailed in § 3. The separate influence of the radius ratio and density contrast are commented for modes up to $m = 6$. In § 4, high-Reynolds-number numerical simulations are carried out beyond the linear stage. Based on these simulations, we describe the main features of the breakdown of a heavy vortex submitted to optimal perturbations with $m = 2$ and $m = 3$.

2. The statement of the problem

2.1. *Equilibrium solutions to the variable-density Euler equations*

In the description of inviscid incompressible flows under negligible gravity, the Navier–Stokes equations reduce to the Euler momentum equations supplemented with a purely convective continuity equation for the density:

$$\nabla \cdot \boldsymbol{u} = 0, \tag{2.1a}$$

$$\mathrm{d}_t \boldsymbol{u} = -\frac{1}{\rho}\nabla P, \tag{2.1b}$$

$$\mathrm{d}_t \rho = 0, \tag{2.1c}$$

where $\mathrm{d}_t = \partial_t + (\boldsymbol{u}\cdot\nabla)$ stands for the material derivative. Let $\boldsymbol{\chi} = \nabla \times \boldsymbol{u}$ be the vorticity that reduces to $(0, 0, \xi)$ in the two-dimensional case. Taking the curl of (2.1*b*) yields the transport equation for the vorticity scalar field

$$\mathrm{d}_t \xi = \boldsymbol{a} \times \frac{\nabla \rho}{\rho} = \boldsymbol{a} \times \nabla(\ln \rho/\rho_0), \tag{2.2}$$

where $\boldsymbol{a} = \mathrm{d}_t \boldsymbol{u}$ is the acceleration of the particle along a streamline and hereinafter the specific density gradient is quoted as $\boldsymbol{g} = \nabla(\ln \rho/\rho_0)$ where ρ_0 can be any density reference. The right-hand side of (2.2) exhibits one source term in contrast to the conservative nature of vorticity in homogeneous two-dimensional inviscid flows. The baroclinic torque $b = \boldsymbol{a} \times \boldsymbol{g}$ is felt when an inhomogeneous mass field is subjected to an acceleration not aligned with the local density gradient. A two-dimensional vortex with circulation Γ and characteristic radius δ is unsensitized to the gravity field if the inertia force due to the vortex flow itself, $\rho u_\theta^2/\delta$ with $u_\theta \sim \Gamma/\delta$ a characteristic azimuthal velocity, is large compared to the projection $g'\Delta\rho$ of the buoyancy force on the vortex plane with $\Delta\rho$ a characteristic density difference between the vortex core and its surroundings. Defining the density contrast as $C_\rho \sim \Delta\rho/\rho$, we form the Froude number $Fr = \Gamma^2/(\delta^3 C_\rho g')$ and we consider $Fr \gg 1$.

A steady solution to the constant-density Euler equation will stand as a solution to the variable-density Euler equations if the density gradient is everywhere aligned with the pressure gradient and isopycnic or isodensity lines are globally invariant by advection. This is verified for any axisymmetric vorticity field associated with any centred axisymmetric density distribution where the baroclinic torque remains inactive as rings of fluid are moving around the vortex centre on circular streamlines. We explore the effect of the density distribution on the stability characteristics of such equilibrium solutions that we term *barotropic vortices*. In the unperturbed diffusive situation, an initially barotropic vortex evolves as a barotropic vortex with the Schmidt number setting the relative spreading rate of density and vorticity fields.

2.2. *The baroclinic torque distribution on a perturbed barotropic vortex*

The purpose of this section is to give a heuristic explanation of the instability mechanism occurring on a high-density barotropic vortex. We give the expression of the baroclinic vorticity production resulting from an harmonic deformation of the otherwise circular density contours. The instability mechanism is demonstrated by considering vorticity sources and sinks as secondary vortices due to the loss of barotropy. We consider a Gaussian axisymmetric vortex of circulation Γ and core radius δ, defined by its vorticity in polar coordinates,

$$\Omega(r, \theta) = \frac{\Gamma}{\pi\delta^2} \exp\left(-\frac{r^2}{\delta^2}\right). \tag{2.3}$$

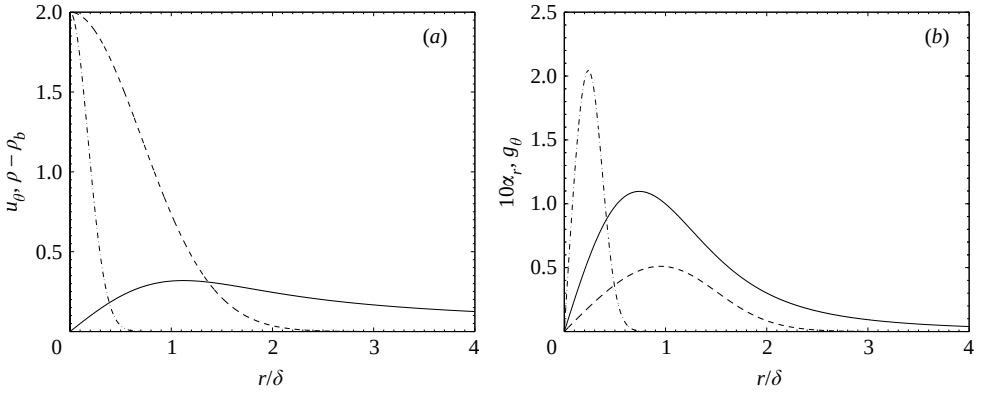

FIGURE 1. Radial profiles along ray $\theta = \pi/4$ of two perturbed dense barotropic vortices with $\Gamma = \pi$, $\delta = 1$, $\rho_c/\rho_b = 3$, $m = 2$ and $e = 0.3$: (*a*) azimuthal velocity u_θ (solid) and density profile $\rho - \rho_b$ for $\varepsilon = 1$ (dashed) and $\varepsilon = 4$ (dot-dashed); (*b*) radial acceleration a_r (solid) and azimuthal component of the specific density gradient g_θ for $\varepsilon = 1$ (dashed) and $\varepsilon = 4$ (dot-dashed).

This vortex induces a purely azimuthal velocity u_θ and a purely radial acceleration a_r,

$$u_\theta(r,\theta) = \left[1 - \exp\left(-\frac{r^2}{\delta^2}\right)\right]\frac{\Gamma}{2\pi r}, a_r(r,\theta) = -u_\theta^2/r. \tag{2.4}$$

In order to obtain a tractable expression of the baroclinic torque in a particular case, we apply a harmonic deformation with amplitude $e < 1$ and azimuthal wavenumber $m > 0$ on a Gaussian axisymmetric density field with characteristic radius $\delta_\rho = \delta/\varepsilon$,

$$\rho(r,\theta) = \rho_b + (\rho_c - \rho_b)\exp\left(-\frac{r_\rho^2(\theta)}{\delta_\rho^2}\right), r_\rho(\theta) = r[1 + e\cos(m\theta)] \tag{2.5}$$

where ρ_b is the density of the background fluid and ρ_c the density at the vortex centre. Hence, the azimuthal component of the specific density gradient reads

$$g_\theta(r,\theta) = \frac{1}{r\rho}\frac{\partial\rho}{\partial\theta} = \left(1 - \frac{\rho_b}{\rho}\right)\frac{2mer}{\delta_\rho^2}[1 + e\cos(m\theta)]\sin(m\theta). \tag{2.6}$$

The radial profiles of these flow variables are illustrated on figure 1 for $m = 2$ and along the ray $\theta = \pi/4$ where g_θ is maximum and for two radius ratios $\varepsilon = 1$ and $\varepsilon = 4$. Increasing the radius ratio concentrates mass towards the vortex core and increases the peak value of g_θ while the radius of maximum gradient decreases.

The deformation of isopycnic lines yields the misalignment between density and pressure gradients resulting in the distribution, b, of baroclinic vorticity sources and sinks

$$b(r,\theta) = a_r\, g_\theta = 2\,m\,e\,\varepsilon^2\frac{u_\theta^2}{\delta^2}\,[1 + e\cos(m\theta)]\,\frac{\rho_b - \rho}{\rho}\,\sin(m\theta). \tag{2.7}$$

The baroclinic torque is of the sign of $(\rho_b - \rho_c)\sin(m\theta)$ and its amplitude increases with the amplitude e of the isopycnic deformation, the azimuthal wavenumber m, the density contrast $(\rho_b/\rho_c - 1)$ and the circulation Γ. Both denser and less-dense vortices are considered in figure 2, where we illustrate the sign of vorticity sources and sinks in the four quadrants of the vortex perturbed on mode $m = 2$. On the interval $\theta \in [0, 2\pi[$, the sign of $\sin(m\theta)$ changes on $(2m - 1)$ rays. Therefore, a system of $2m$ alternate sign contributions corresponding to m counter-rotative dipoles are superimposed on

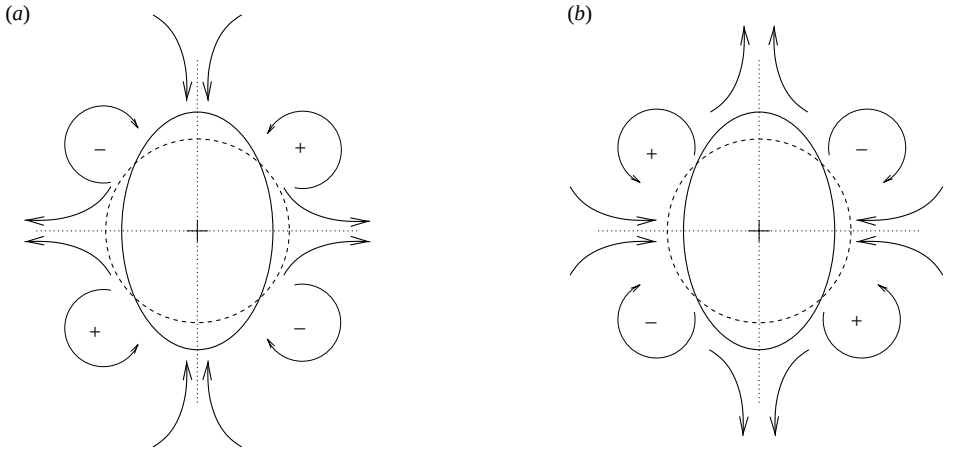

FIGURE 2. Sketch of the baroclinic torque contributions on Gaussian vortices bearing (*a*) less-dense and (*b*) denser elliptic density distributions. - - -, vorticity contour; —, density contour.

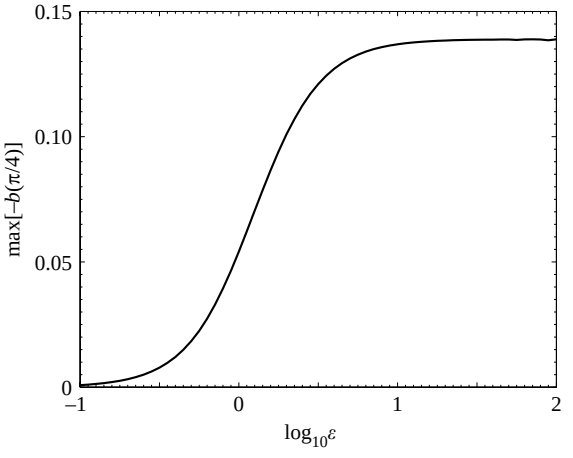

FIGURE 3. Maximum of the negative baroclinic vorticity source at $\theta = \pi/4$ versus the radius ratio $\varepsilon = \delta/\delta_\rho$ for a barotropic vortex with $\Gamma = \pi$, $\delta = 1$ and $\rho_c/\rho_b = 3$ with the density radius deformed with $m = 2$ and $e = 0.3$.

the base vorticity field. Consequently, less-dense fluid particles are engulfed in and denser fluid particles are ejected from the vortex core between consecutive dipoles. Axisymmetrization of the density distribution is expected if the vortex core is less dense than the surrounding fluid, whereas vortices with a denser core are unstable to perturbations. The arbitrary harmonic deformation of the density field serves here as an illustration of the generic distribution of vorticity sources and sinks on a perturbed barotropic vortex. The instability of the massive vortex is the result of the departure from barotropy or, as developed in § 2.1, proceeds from the loss of axisymmetry. The sensitivity of the baroclinic torque intensity to the mass-concentration ε towards the vortex axis is described in figure 3 in the case of a dense vortex. The harmonic deformation of the density isocontours indicates that the Rayleigh–Taylor instability

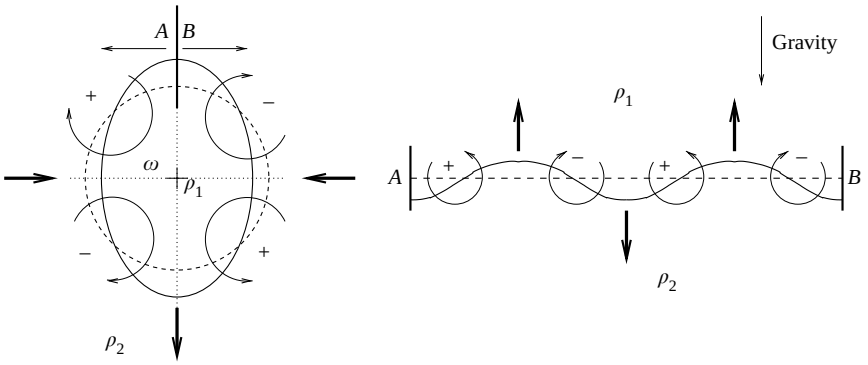

FIGURE 4. Analogy between the dense vortex and the unstable density stratification submitted to a downward gravity field ($\rho_1 > \rho_2$). —, density contour (isopycnic); - - -, vorticity contour.

of the denser vortex is favoured by a characteristic density radius smaller than the vorticity radius.

This mechanism is similar to that occurring in Rayleigh–Taylor instability where a quiescent stratified medium is submitted to the external acceleration of the gravity field. There, the acceleration is of constant direction and intensity, and the stability of the flow is governed by the misalignment between a fixed acceleration field and a perturbed density gradient. Here, the acceleration field is due to the kinematics of the vortex flow which initially yields a purely radial acceleration. Figure 4 illustrates the analogy between the unstable atmosphere and the equivalent unrolled heavy vortex. This is the basic mechanism mentioned by Turner (1957) and observed in another context by Miller *et al.* (2003). Now we explore the parameter space of the isolated dense vortex with a normal mode linear stability analysis.

2.3. *The equations for the inviscid stability analysis*

The base flow is the Gaussian vortex with azimuthal velocity $U(r)$ as given by (2.4). We superimpose the following density distribution $R(r)$ also resulting from similarity solutions of the diffusive problem,

$$R = \rho_b + (\rho_c - \rho_b)\exp\left(-\frac{r^2}{\delta_\rho^2}\right). \tag{2.8}$$

We choose the density contrast $C_\rho = (\rho_c - \rho_b)/(\rho_c + \rho_b)$ as the relevant parameter, lying in $[-1, 1]$, to explore the whole range of density ratios. This parameter, elsewhere invoked as an Atwood number, gives a straightforward logarithmic scale for the normalization of relative density gradients in the equations. Denoting $s = \rho_c/\rho_b$ the density ratio, both measures of the fluid inhomogeneity are, of course, equivalent by $C_\rho = (s-1)/(s+1)$. Besides, the radius of the density Gaussian distribution provides a second length scale δ_ρ that will be related to the vorticity radius by the ratio $\varepsilon = \delta/\delta_\rho$. We will often refer to vortices larger then their associated density field for which $\varepsilon > 1$.

The variable-density Euler equations are linearized around the base flow for the velocity, pressure and density perturbations $[\hat{u}_r, \hat{u}_\theta, \hat{p}, \hat{\rho}](r, \theta, t)$. The perturbations are assumed to be of the form $[\hat{u}_r, \hat{u}_\theta, \hat{p}, \hat{\rho}] = [\mathrm{i}u_r(r), u_\theta(r), p(r), \rho(r)]\exp[\mathrm{i}(m\theta - \omega t)]$, where m is the positive integer azimuthal wavenumber and ω is the complex disturbance phase speed. With $\gamma = mU/r - \omega$, $()^* = ()' + ()/r$ and prime denoting

r-differentiation, we write the set of equations for the disturbance amplitudes:

$$\gamma\rho + R'u_r = 0, \tag{2.9}$$

$$u_r^* + mu_\theta/r = 0, \tag{2.10}$$

$$R(\gamma u_r + 2Uu_\theta/r) + U^2\rho/r + p' = 0, \tag{2.11}$$

$$R(\gamma u_\theta + U^* u_r) + mp/r = 0. \tag{2.12}$$

The loss of barotropy being associated with the loss of axisymmetry, there are no unstable modes for axisymmetric perturbation and hereinafter $m > 0$. The eigenfunctions must vanish at $r = \infty$, and considering leading-order terms in the Taylor series we obtain the limit behaviour at $r = 0$:

$$u_r, u_\theta \sim O(r^{m-1}), \quad p, \rho \sim O(r^m). \tag{2.13}$$

We reduce the system (2.9)–(2.12) to a minimalist set of two coupled equations for the amplitudes of the radial velocity and the density perturbations:

$$\gamma\rho + R'u_r = 0, \tag{2.14}$$

$$(r^2 R\gamma/m)u_r'' + [2RU + r(rR\gamma)'/m + 2rR\gamma/m - rRU^*]u_r' + [2RU/r - mR\gamma - (rRU^*)' + (rR\gamma)'/m]u_r + (mU^2/r)\,\rho = 0. \tag{2.15}$$

Included in the function γ, the phase speed $\omega = \omega_r + \mathrm{i}\omega_i$ appears linearly in the above system which forms an eigenvalue problem. The sign of the imaginary part of ω discriminates between stable vortices for negative ω_i and unstable vortices for positive ω_i.

We use a spectral collocation method on a basis of Chebyshev polynomials mapped algebraically on the interval $[0, \infty]$. This discretization produces a generalized eigenvalue problem under the matrix form $\boldsymbol{A}\boldsymbol{x} = \omega\boldsymbol{B}\boldsymbol{x}$ that is solved by the QZ algorithm under Matlab. The number of Chebyshev modes for each variable is N which sets the dimension of matrices $\boldsymbol{A}$ and $\boldsymbol{B}$ to $(2N)^2$. Owing to the presence of critical layers where $\gamma = 0$, the search of the frontier of neutral stability requires contouring the singularities in the complex plane (see Boyd 1985). Increasing the number of collocation points shrinks the discretization spectrum towards the real axis, but does not succeed in unveiling the neutral limit. We use contour deformation according to the proposal of Leibovich & Stewartson (1983) which deforms the discretization spectrum below the real axis. The real coordinate r is mapped to $\hat{r} = r[1 - \mathrm{i}\lambda\gamma'(r)]$, where $\lambda \in [0, 1]$ sets the intensity of the contour deformation. All real coefficients of the system (2.14), (2.15) are made complex by substitution of $\hat{r}$ to r. For the detection of the most amplified mode, we increase simultaneously the number of collocation points N and the displacement factor λ until one fixed point is detected in the (ω_r, ω_i)-plane. The invariance to the couple (N, λ) is judged to a relative accuracy of 10^{-4}. This results in rapid convergence and $N \sim 60$ for largely amplified modes remote to the neutral limit whereas marginally stable modes require a higher resolution raising up to $N \sim 300$.

3. Topography of the instabilities

Figure 5 displays the contours of the amplification rate in the (C_ρ, ε)-plane for modes $m = 2$ and $m = 3$ and positive values of the density contrast. As expected from the above considerations, no unstable modes are found for vortices less dense then the background fluid, i.e. for negative C_ρ. We choose to apply a logarithmic scale

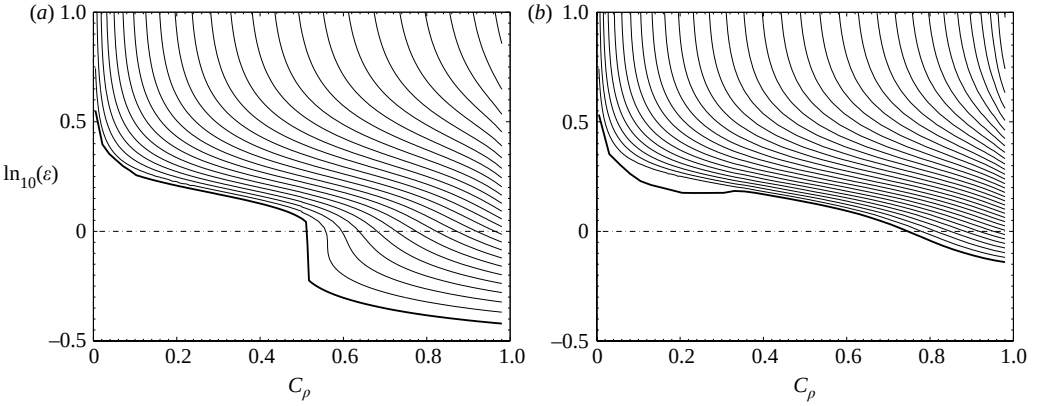

FIGURE 5. Contours of constant amplification rate ω_i in the $(C_\rho, \ln_{10}(\varepsilon))$-plane for azimuthal wavenumbers (*a*) $m = 2$, $m = 3$. (*b*) The increment between contours is 0.02 and the thick line is the neutral curve.

to the radius ratio to stretch the range around unity. For $m = 2$, the neutral curve stands above $\varepsilon = 1$ for density contrasts below 0.5. The sharp transition around this value is due to weakly amplified modes detected for extremely dense vortices. For this azimuthal wavenumber, the amplification rate peaks up to 0.48 in the upright corner of the (C_ρ, ε)-plane. The map of the amplification rate for $m = 3$ is similar with a maximum amplification rate of 0.62 for unrealistic extreme density ratios ($C_\rho \sim 1$) and very small density cores ($\varepsilon \gg 1$).

Given a density contrast, the vortex is stable to small perturbations below a critical radius ratio. For moderate density ratios encountered in binary mixing and thermal mixing, instability will occur only if the denser core is smaller than the vortex core. This must be related to the preliminary results displayed on figure 3, stressing the increase of the perturbation baroclinic torque with decreasing density radii. For a given density contrast, the density gradient increases when reducing the density radius and so does the cause of the Rayleigh–Taylor instability. For small enough dense cores, the growth rate of the instability in the linear regime increases with the density contrast. Consequently, the larger growth rates are found in the upper right-hand corner of the (C_ρ, ε)-plane.

These main conclusions are further illustrated in figure 6 where we separate the influences of the radius ratio and the density contrast for the first six modes. For a mean density contrast $C_\rho = 0.5$, the critical radius ratio is seen to increase with the azimuthal wavenumber. The increase of the growth rate with increasing radius ratio saturates before $\varepsilon = 10$ when only one length scale, δ, becomes relevant to the base flow. The asymptotic value at saturation is seen to increase with the azimuthal wavenumber. As seen for modes 2 and 3, the amplification rate increases with the density contrast for a given radius ratio. It is seen from figure 6 that for a radius ratio $\varepsilon = 2$, mode $m = 2$ is the most unstable for moderate density contrasts below 0.35 and is superseded by mode $m = 3$ above that level.

Mode $m = 1$ exhibits much lower amplification rates than modes $m = 2$ and $m = 3$ almost everywhere except in a small region of the parameter space lying around $(C_\rho, \varepsilon) = (0.2, 1.4)$. As also displayed in a complementary paper by Sipp *et al.* (2005), we found that when mode $m = 1$ is the most amplified mode, its amplification rate remains below 0.01. From Joly & Reinaud (2005), it is seen that vortex interactions

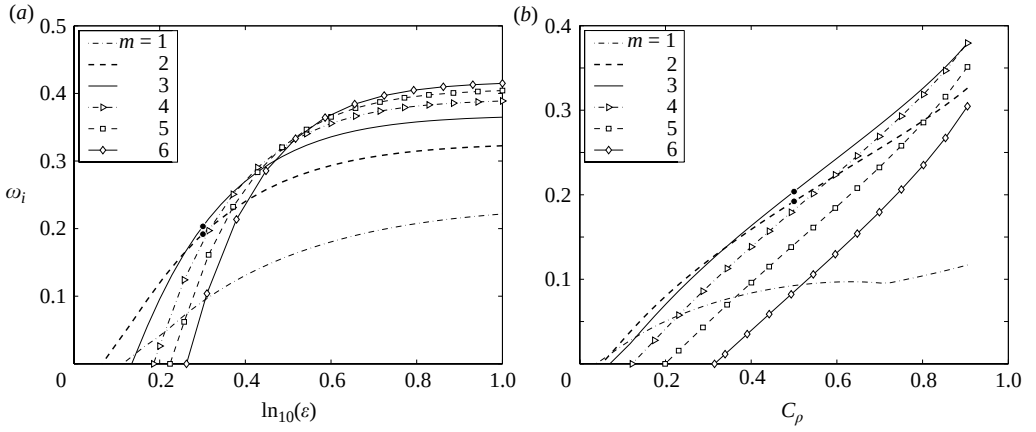

FIGURE 6. Analysis of the separate influence of the radius ratio and the density contrast on the amplification rate ω_i of the first six azimuthal wavenumbers. (*a*) Influence of the radius ratio for a density contrast $C_\rho = 0.5$ corresponding to a core 3 times denser then the surrounding fluid; (*b*) influence of the density contrast for a radius ratio $\varepsilon = 2$. The black dots on both figures locate the modes selected for the nonlinear simulations.

m	1	2	3	4	5	6	7
ω_i	0.094760	0.192196	0.20379	0.18209	0.14101	0.08519	0.01666
ω_r	0.297621	0.734845	1.20582	1.67331	2.14001	2.60726	3.07500

TABLE 1. Eigenvalues for the unstable mode of the vortex defined by $C_\rho = 0.5$ and $\varepsilon = 2$.

occurring in a typical two-dimensional vortex merger are producing large-scale perturbations similar to the $m = 2$ case. We focus here on these largely amplified modes likely to occur in viscous flows with vortex interactions.

From these results we select the vortex with a density core half the size of the vortex core, $\varepsilon = 2$, and $C_\rho = 0.5$, corresponding to a density ratio of $s = 3$. This vortex is unstable to modes $m = 1$ to $m = 7$ with eigenvalues reported in table 1. The absolute value of the eigenfunctions of velocity and density perturbations is described in figure 7 for modes $m = 2, 3, 4, 6$. The asymptotic behaviour at the origin as prescribed by 2.13 is verified. In particular, the velocity eigenfunctions of mode $m = 2$ exhibit a linear growth from the origin. As m is increased, the velocity and density eigenfunctions spread over a region of narrowing radial extent. This region is centred on the characteristic radius $r = \delta_\rho$ of the density distribution. The spatial structure of these modes is compared in figure 8 displaying the two-dimensional vorticity perturbation fields. The vorticity perturbation and density perturbation (not displayed) are organized as $2m$ spiral arms of alternate sign. In the next section, we investigate the development of eigenmodes $m = 2, 3$ beyond the linear stage.

4. Nonlinear simulations of the breakdown of a dense vortex

4.1. *The numerical procedure*

A viscous numerical simulation is carried out on the previously selected base field perturbed by the most unstable inviscid mode. In the limit of zero Mach number, the

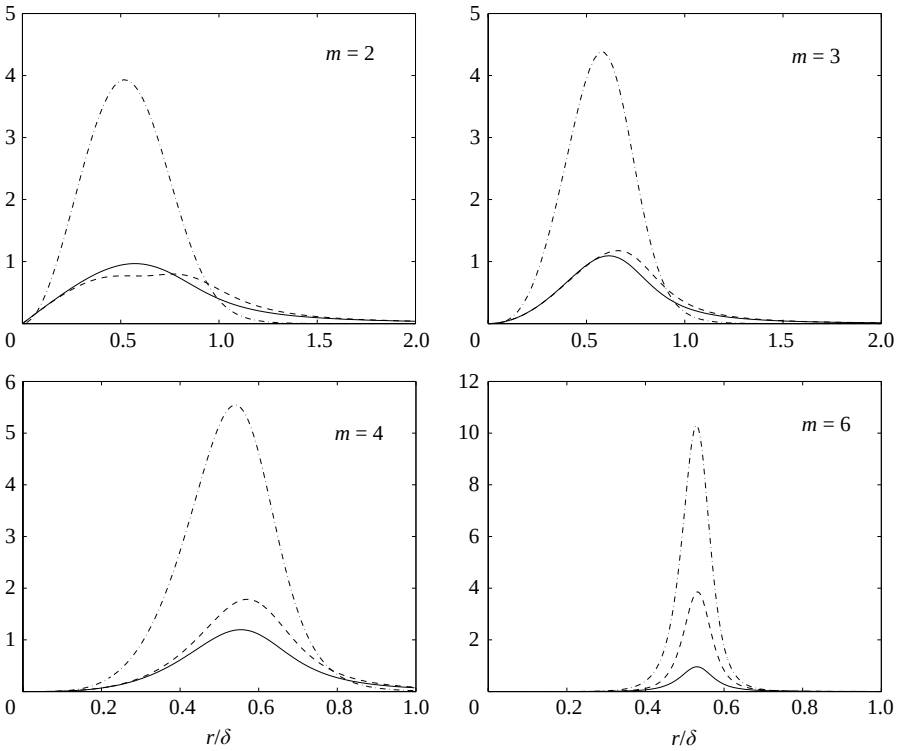

FIGURE 7. Absolute value of the eigenfunctions of the denser vortex flow with $C_\rho = 0.5$ and $\varepsilon = 2$: radial velocity u_r (solid), azimuthal velocity u_θ (dashed) and density ρ (dot-dashed). Normalization is performed to ensure a unitary kinetic energy $e = \frac{1}{2}\int_0^\infty (u_r^2 + u_\theta^2)\,\mathrm{d}r$.

divergence of the velocity field is due to the molecular diffusion of species only, and the continuity equation comes out as an advection–diffusion one. This is relevant to the mixing of two incompressible fluids with Fickian diffusion allowing the density to vary between the densities of the pure species, ρ_c and ρ_b. For the high-Reynolds-number flows considered here, the divergent contribution of the viscous diffusion is discarded. We consider also constant diffusivities in order to retain first-order density effects of inertial nature in a minimalist code avoiding contributions due to variations of the fluid properties, see Chassaing *et al.* (2002) for details. The characteristic scales are determined by the vortex circulation Γ, the vortex radius, the density contrast and the radius ratio. In particular, the time scale τ is the inverse of the maximum vorticity $\pi\delta^2/\Gamma$. Given a unitary Schmidt number and $Re = \Gamma/\nu = 20\,000$ the Reynolds number based on the vortex circulation Γ, we solve the following normalized transport equations for the primitive variables $(\varrho, \boldsymbol{u})$, with $\varrho = \ln(\rho/\rho_b)$,

$$\mathrm{d}_t \varrho = \frac{1}{ReSc}\Delta\varrho, \tag{4.1a}$$

$$\mathrm{d}_t \boldsymbol{u} = -\frac{1}{\rho}\nabla p + \frac{1}{Re}\Delta\boldsymbol{u}. \tag{4.1b}$$

The numerical procedure is a two-thirds dealiased pseudo-spectral code based on a variable-density transpose of the projection method ensuring the diffusive nature of the velocity divergence. The non-solenoidal part of the velocity field is prescribed when

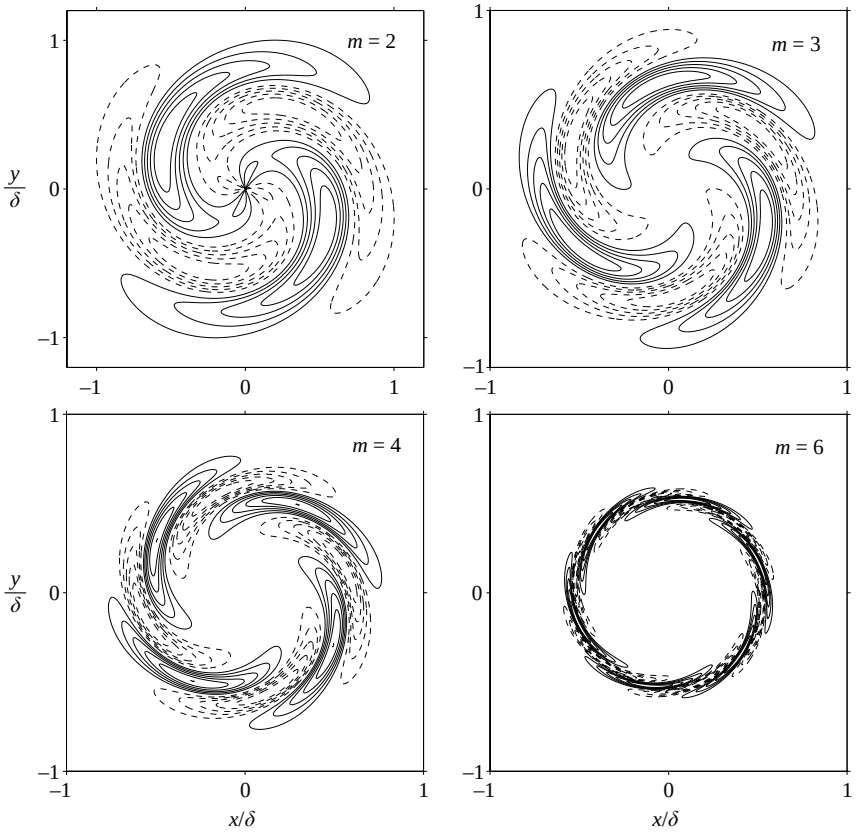

FIGURE 8. Two-dimensional structure of the vorticity perturbation corresponding to eigenmodes $m = 2, 3, 4, 6$ of the vortex with $C_\rho = 0.5$ and $\varepsilon = 2$. Contour spacing : $\max(\hat{\xi})/6$.

solving the Poisson equation for the pressure by ensuring: $Re\,Sc\nabla\cdot\boldsymbol{u} = -C_\rho\Delta\varrho$. The variables are time-advanced using a low-storage third-order Runge–Kutta scheme with semi-implicit treatment of right-hand-side terms. The time step is variable and adjusted according to the current maximum of velocity ensuring the Courant–Friedrichs–Lewy condition is respected with $\mathrm{CFL} = \Delta t/\Delta x \times \max(u)$ kept under 0.7. As will be described later, the spatial structure of the flow evolves towards much smaller length scales. We opted for a time-dependent spatial resolution to minimize the early-time simulation cost. Starting with a 2048^2 grid, a spectral sensor placed near the maximum wavenumber triggers the increase of the spectral radius raising the final resolution up to 5760^2 in the $m = 3$ case. At the initial time, the amplitude of the perturbation is normalized to represent 2 % of the enstrophy of the base flow.

The boundary conditions are periodic in both directions, resulting in a bias compared to the case considered in the stability analysis with an infinite spatial extent. As discussed by Pradeep & Hussain (2004), periodicity of the boundary conditions yields zero normal and tangential velocities on the square computational boundaries and a zero circulation over the computational domain. Owing to its slow radial decrease, the azimuthal velocity of the base flow is the variable most affected by this constraint. A background negative value ξ_b such that $\xi_b \times L_x \times L_y = -\Gamma$ is also added to the vorticity field. The bias amplitude depends on the relative size of the computational domain compared to the vortex core. In the simulations commented

on here, the vortex circulation is $\pi/4$ while the domain is $(2\pi)^2$ with a vortex radius $\delta = 0.5$. This corresponds to a distance from the vortex centre to the domain boundary of a little more than 6 radii and a peak vorticity $\xi_p = 1 + \xi_b$. In this case, $\xi_b = (16\pi)^{-1}$ which amounts to less than 2 % of ξ_p. This allows for a good compromise between representing the isolated vortex flow and the required spatial resolution of the very thin layers arising during the nonlinear stage of the instability. However, clearly, the eigenmodes deduced from the stability analysis only approach the eigenmodes of the effective base flow as seen from the numerical simulation tool. The simulation of the linear stage thus suffers from the lack of representivity of the boundary conditions of the isolated vortex. However, in the nonlinear stage, the instability mechanism produces baroclinically enhanced vorticity up to 10 times the initial peak value ξ_p, or 1000 times the artificial background vorticity ξ_b. Simulations were performed in worse conditions with a vortex radius twice the present one and exhibited vorticity and density fields very similar to those that follow. We conclude that the nonlinear stage is properly represented despite the periodization of the flow. Besides, the purpose of this numerical approach is to give a first illustration of this original instability mechanism beyond the linear stage.

4.2. *Description of the flow*

Figures 9–12 illustrate the time evolution of the vorticity and density fields of nonlinear realizations of the Rayleigh–Taylor instability for modes $m = 2$ and $m = 3$ of the vortex three times denser than the surrounding fluid. As the instability develops, the baroclinic torque concentrates vorticity on m spiral arms while it destroys it in-between. These spiral arms are turning into vorticity sheets of decreasing thickness and increasing vorticity. The centre of the vortex is gradually mass-deprived as dense fluid particles initially in the vortex core are ejected away on the spiral arms. These vorticity sheets partially roll up into m smaller vortices associated with densities much smaller than the initial core density. Beside the breakdown process and the condensation on smaller vortices, vorticity filaments of both signs are generated and wrapped around emerging more robust vortices.

Let Ω be the vorticity of the base flow given by (2.3). We measure the amplitude of the vorticity and density perturbations by,

$$\xi' = \int (\xi - \Omega)\,\mathrm{d}x\,\mathrm{d}y, \qquad \rho' = \int (\rho - R)\,\mathrm{d}x\,\mathrm{d}y. \tag{4.2}$$

The radius of the unperturbed Gaussian vortex is known to evolve as $\delta = \delta_0\sqrt{1 + 4\pi t/Re}$ in normalized time units. Considering the very high Reynolds number of the simulation, the radius of the unperturbed field would have gained less than 1 % of the initial value at $t = 20$. Figure 13 displays the time evolution of the perturbation amplitudes, normalized by their initial value. The exponential growth rates of these perturbations as predicted by the linear stability analysis are $\sigma_{m=2} = 0.192$ and $\sigma_{m=3} = 0.204$. We compare the effective growth rates to an average growth rate $\sigma = 0.2$. The vorticity and density perturbations are seen to grow after a few time units because of the non-optimal nature of the eigenmodes within the numerical frame. Then exponential growth is observed that compares well with the predicted rate despite the misrepresentation of the boundary conditions. In figure 13(*b*), the density perturbation of mode $m = 3$ is seen to grow faster than the density perturbation of mode $m = 2$, confirming the slight precedence of mode $m = 3$. From the evolution of the amplitude of vorticity and density perturbations, the saturation is seen to occur

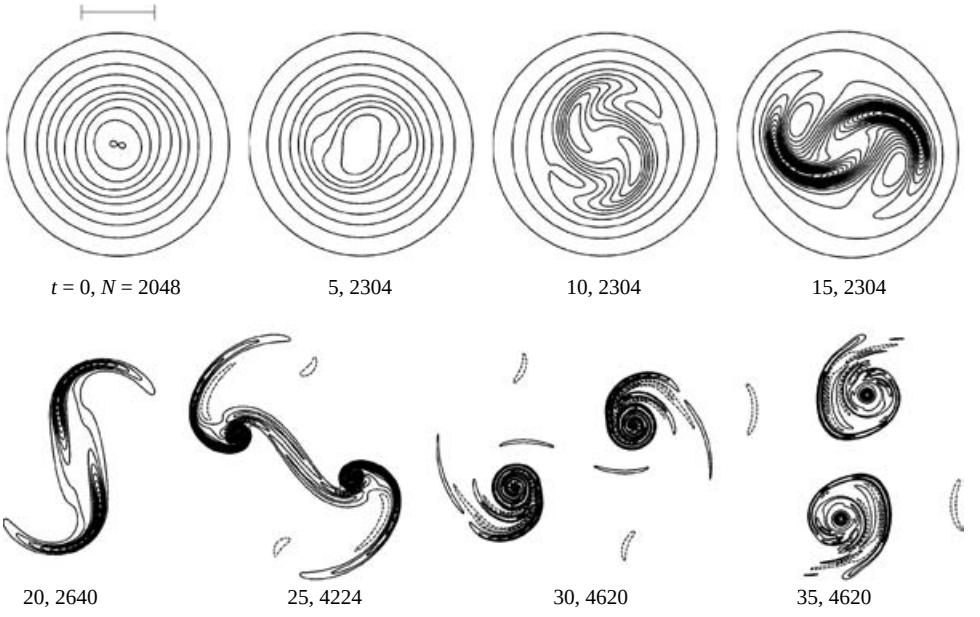

FIGURE 9. Sequence of isovorticity contours for $m = 2$. Length scale δ is represented by the line segment at $t = 0$. Contour spacing $0.1/\tau$ from $t = 0, 5, 10, 15$, $0.4/\tau$ for $t = 20, 25$ and $0.8/\tau$ for $t = 30, 35$. Contours at negative levels are dashed. N is the number of grid points along one direction of the squared simulation domain.

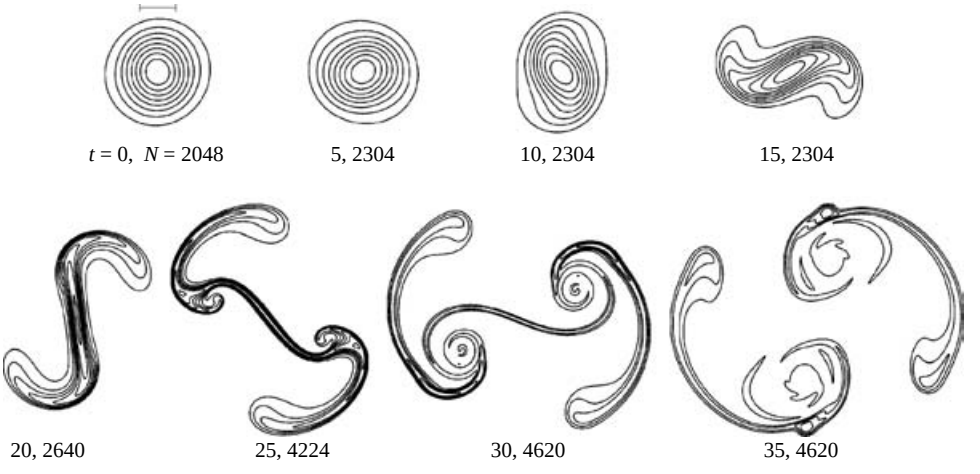

FIGURE 10. Sequence of isodensity contours for $m = 2$. Length scale δ_ρ is represented by the line segment at $t = 0$. Fixed contour spacing $(\rho_c - \rho_e)/9$.

near $t = 30$ for both modes. The departure from the linear exponential growth is effective by $t = 20$.

In figure 14(a), enstrophy production by the baroclinic torque is seen to peak at saturation time. The peak value is higher for mode $m = 2$ and approximately six times the initial value. In the development of mode $m = 3$, a secondary instability of the vortex sheets results in a small burst of enstrophy at $t = 35$. Then for both modes, the enstrophy monotonously decreases owing to viscous dissipation at high wavenumbers.

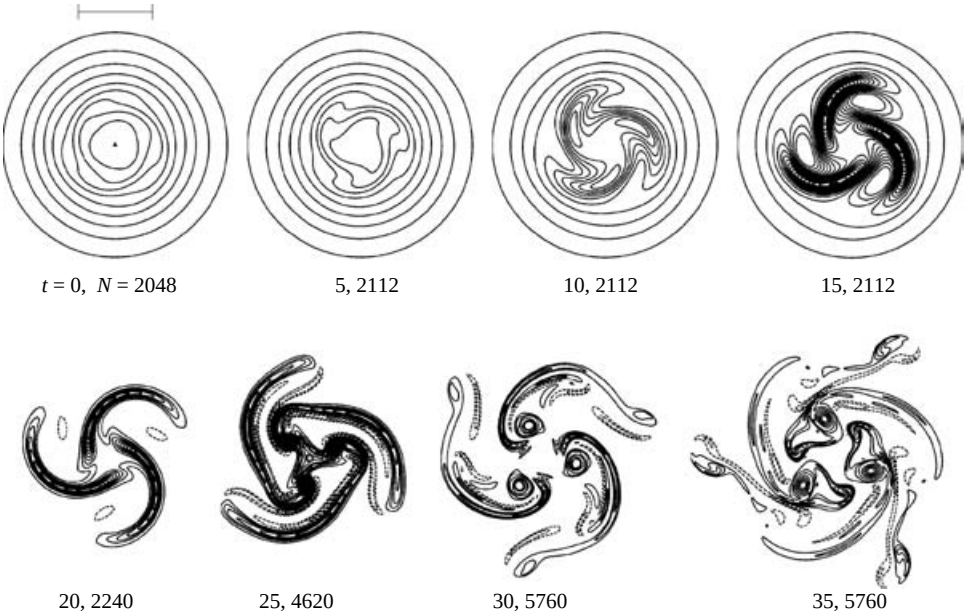

FIGURE 11. Sequence of isovorticity contours for $m = 3$. Legend as for $m = 2$ in figure 9.

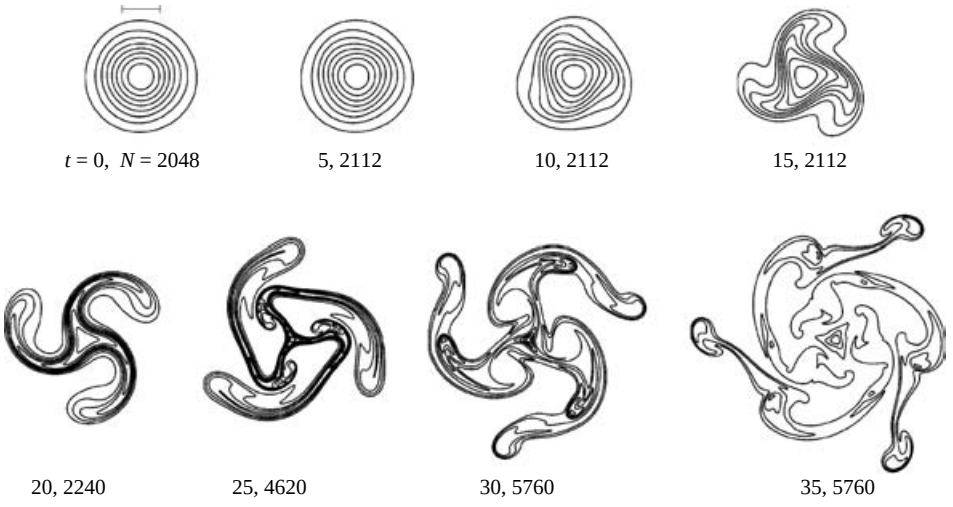

FIGURE 12. Sequence of isodensity contours for $m = 3$. Legend as for $m = 2$ in figure 10.

The baroclinic vorticity generation has been proposed as the basic mechanism of this instability, in yielding the centrifugal ejection of the denser fluid particle away from the vortex core. In order to prove this point, we measure the correlation between the radial velocity and the density difference relative to the mean density $\bar{\rho}$, where the overbar denotes an average over the whole simulation domain. The correlation is normalized by their respective variances to form a correlation coefficient,

$$\mathscr{C}_{\rho u_r} = \frac{\overline{(\rho - \bar{\rho}) u_r}}{\left(\overline{(\rho - \bar{\rho})^2}\ \overline{u_r^2}\right)^{1/2}}. \tag{4.3}$$

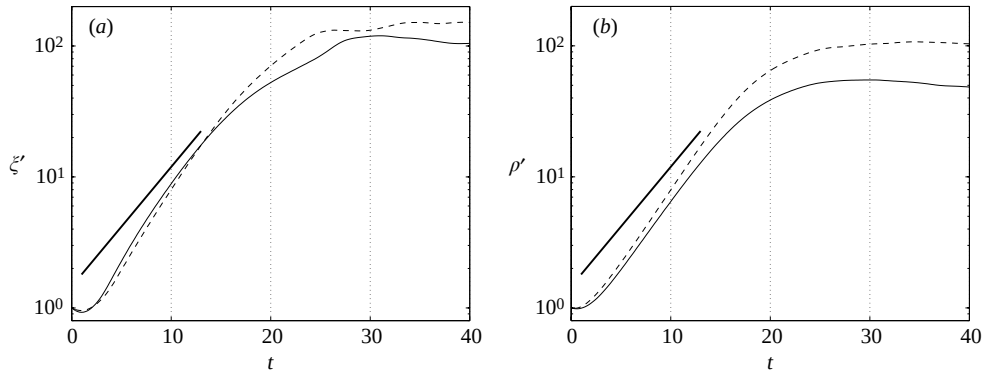

FIGURE 13. Time evolution of the normalized amplitude of the vorticity perturbation (a) and of the density perturbation (b) for modes $m = 2$ (solid), $m = 3$ (dashed). The thick solid line represents an exponential growth with a rate averaged between $m = 2$ and $m = 3$ growth rates predicted by the linear stability analysis, i.e. $\sim \exp(0.2t)$.

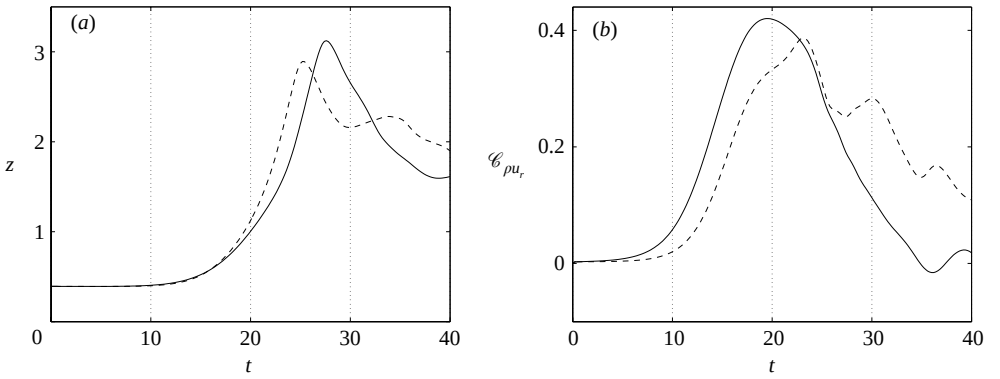

FIGURE 14. (a) Time evolution of the total enstrophy on the simulation domain $z = \int \xi^2 \, \mathrm{d}x \, \mathrm{d}y$. ($b$) Time evolution of the correlation coefficient between the density fluctuation and the radial velocity.

From the time evolution of this correlation coefficient in figure 14(b), the ejection of high-density fluid particles and convergence of low-density ones towards the vortex centre is seen to be significant after several time units. It occurs sooner for mode $m = 2$ and reaches a value of 0.4 well before saturation time, indicating a coherent mass ejection as seen from density isocontours on figure 10 at $t = 20, 25$. After the two smaller vortices have formed far from the centre of the domain, the radial velocity is not relative to a vortex centre and $\mathscr{C}_{\rho u_r}$ is no longer relevant. Mass ejection during the nonlinear development of mode $m = 3$ is less violent and occurs later in two phases associated with the two peaks in enstrophy generation. After the first stage between $t = 20$ and $t = 25$, three small vortices are seen to rotate near the initial vortex centre in figure 11 at $t = 30$. At this point, the radial velocity from the domain centre is still relevant to the global vortex system. Then another centrifugal mass ejection is observed by $t = 30$ signalled by a second increase of enstrophy and $\mathscr{C}_{\rho u_r}$.

The measure of the density at the centre of the m smaller structures at $t = 30$ reveals a density ratio of $s = 1.44$ against the background medium, corresponding to a density contrast $C_\rho = 0.18$. Owing to the unitary Schmidt number the resulting

roll-ups have similar density and vorticity radii, hence $\varepsilon \sim O(1)$. We refer to figure 5 to conclude that these new vortices, slightly denser than the surrounding fluid, are stable pertaining to the Rayleigh–Taylor instability. From inspection of the contours of figures 10 and 12, we estimate that the characteristic length scale of the m generated vortices compared to the initial vorticity radius has been divided by 6 for $m = 2$ and by 10 for $m = 3$. Moreover, very high levels of vorticity have been generated and the chosen values at the new vortex centres are ten times higher than the initial maximum vorticity for both cases. A clear picture of the situation after the completion of the Rayleigh–Taylor instability then emerges from these measurements. The baroclinic production of vorticity has produced smaller stable roll-ups of much higher vorticity. During the process, high-density samples of fluid have been shed forming strained lumps much more sensitive to molecular diffusion than the initial barotropic distribution.

5. Concluding remarks

The analysis of the linear inviscid stability of the variable-density isolated vortex has been derived. The heavy vortex is subjected to a Rayleigh–Taylor instability promoted by the concentration of dense fluid on a smaller radius than the vortex core. Low azimuthal wavenumbers, $m = 2, 3$ are seen to be more amplified for moderate radius ratios and realistic density ratios. The maps of their growth rates have been established and the neutral curve delineated in the density-contrast versus radius-ratio parameter space. Nonlinear numerical simulations of the breakdown of a vortex three times denser than the surrounding fluid have been carried out for eigen-perturbations derived for $m = 2$ and $m = 3$. The baroclinic torque is seen to produce thinning vorticity sheets partially nucleating into m robust smaller vortices of lower density and higher vorticity than the initial one. This relaxation towards a more stable flow proceeds from vorticity exchange between dense fluid particles from the vortex core and less-dense ones from the background irrotational field.

This mechanism shall be examined further as being central to variable-density mixing at high Froude-number. The instability of high-density vortices and the robustness of low-density vortices are expected to result in mass-segregation by vorticity in two-dimensional flows, resulting in low-density fluid particles near vortex centres and high-density fluid particles occupying the interlacing medium. Measuring the anti-mixing effect of the mass-segregation mechanism should be addressed in turbulent flows where vortex interactions are crucial and lower the relevance of the isolated vortex configuration. However, the spectral reconditioning of the vorticity field towards higher wavenumbers associated to the breakdown of high-density vortices increases dissipation and mixing at small scales. The resulting strained high-density fluid lumps arising during the development of the Rayleigh–Taylor instability are more efficiently smeared out by molecular mass-diffusion. The resolution of these contradictory effects of the baroclinic torque on the mixing efficiency is the subject of ongoing efforts. The influence of the Schmidt number may well be of first importance in the discussion of such a question. In the perspective of variable-density turbulent situations, the two-dimensional and three-dimensional vortex interactions are also under consideration.

We acknowledge fruitful discussions with J. N. Reinaud and D. G. Dritschel. Numerical simulations were performed on the scalar resources of the IDRIS centre under project number 41552.

REFERENCES

Boyd, J. 1985 Complex coordinate methods for hydrodynamic instabilities and Sturm–Liouville eigenproblems with an interor singularity. *J. Comput. Phys.* **57**, 454–471.

Chassaing, P., Antonia, R., Anselmet, F., Joly, L. & Sarkar, S. 2002 *Variable Density Fluid Turbulence*. Kluwer.

Chassaing, P., Castaldi, S., Harran, G. & Joly, L. 1997 Variable density mixing in kinematically homogeneous turbulence. *Eleventh Symp. on Turbulent Shear Flows, 8–10 Sept., Grenoble, France*.

Chomiak, J. & Nisbet, J. R. 1995 Modeling variable density effects inturbulent flames – some basic considerations. *Combust. Flame* **102**, 371–386.

Eckhoff, K. S. 1984 A note on the instability of columnar vortices. *J. Fluid Mech.* **145**, 417–421.

Joly, L. 2002 *Inertia Effects in Variable-Density Flows*. Habilitation à Diriger des Recherches INPT.

Joly, L. & Reinaud, J. 2005 The merger of two-dimensionnal radially-stratified high-Froude number vortices. (In preparation)

Leibovich, S. & Stewartson, K. 1983 A sufficient condition for the instability of columnar vortices. *J. Fluid Mech.* **126**, 335–356.

Miller, P., Lindstrom, P. & Cook, A. 2003 Visualizations of the dynamics of a vortical flow. *Phys. Fluids, Gallery of Fluid Motion* **15** (9).

Monkewitz, P. & Sohn, K. 1988 Absolute instabilities in hot jets. *AIAA J.* **26**, 911–916.

Pradeep, D. & Hussain, F. 2004 Effects of boundary conditions in numerical simulations of vortex dynamics. *J. Fluid Mech.* **516**, 115–124.

Reinaud, J., Joly, L. & Chassaing, P. 2000 The baroclinic secondary instability of the two-dimensional shear layer. *Phys. Fluids* **12**, 2489–2505.

Sipp, D., Fabre, D., Michelin, S. & Jacquin, L. 2005 Stability of a vortex with a heavy core. *J. Fluid Mech.* **526**, 67–76.

Soteriou, M. & Ghoniem, A. 1995 Effects of the free-stream density ratio on free and forced spatially developing shear layers. *Phys. Fluids* A **7**, 2036.

Turner, J. 1957 Buoyant vortex rings. *Proc. R. Soc. Lond.* A **239**, 61.

Turner, J. 1973 *Buoyancy Effects in Fluids*, 2nd edn. Cambridge University Press.